Abstract

[1] showed that rotational acceleration stabilized the leading-edge vortex on revolving, low-aspect-ratio wings, and hypothesized that a Rossby number of around three, which is achieved during each half-stroke for a variety of hovering insects, seeds, and birds, represents a convergent high-lift solution across a range of scales in nature. Subsequent work has verified that, in particular, the Coriolis acceleration plays a key role in LEV stabilization. Implicit in these results is that there exists an optimal aspect ratio for wings revolving about their root, because it is otherwise unclear why, apart from possible morphological reasons, the convergent solution would not occur for an even lower Rossby number. We perform direct numerical simulations of the flow past revolving wings where we vary the aspect ratio and Rossby numbers independently by displacing the wing root from the axis of rotation. We show that the optimal lift coefficient represents a compromise between competing trends with competing time scales where the coefficient of lift increases monotonically with aspect ratio, holding Rossby number constant, but decreases monotonically with Rossby number, when holding aspect ratio constant. For wings revolving about their root, this favors wings of aspect ratio between three and four.

On the lift-optimal aspect ratio of a revolving wing at low Reynolds number

T. Jardin and T. Colonius

May 22, 2018

1 Introduction

Compared to conventional helicopter blades, wings of animal species capable of hovering flight have low aspect ratio, and they operate in the low Reynolds number, separated flow regime. [2] have shown that the aerodynamics of flapping flight mostly rely on the generation of a large-scale leading-edge vortex (LEV). The principal contributor to vortex-lift generation, this LEV forms during each half stroke as the wing revolves through an angle about its root, and it was found to remain stably attached to low aspect ratio wings throughout the whole revolving motion. This is contrary to the LEV that forms on translating wings where the initial LEV is shed into the wake and is typically followed by cyclic vortex shedding, even at low aspect ratio [3]. Recent works by [1] and [4, 5] suggest that the Coriolis acceleration associated with rotation plays a key role in this robust attachment of the LEV. In particular, theoretical considerations suggest that the Coriolis acceleration is accompanied by a spanwise flow behind the LEV [1] that is conducive to spanwise vorticity transport. By balancing the production of vorticity at the leading edge, spanwise vorticity transport limits vortex growth [6] and hence promotes LEV attachment. While this hypothesis is supported by other recent works [7, 8], there is no consensus about the role of Coriolis acceleration on LEV attachment. In particular, [9] do not conclude on the stabilizing or destabilizing effect of the Coriolis acceleration but indicate that the latter drives the spanwise extent of a stable LEV. On the other hand, [10] suggest that Coriolis acceleration has a destabilizing effect and that centripetal acceleration plays a dominant role in LEV attachment. Nevertheless, all studies support the idea that rotational effects promote LEV attachment. Coriolis acceleration, and more generally rotational effects, can be quantified using the Rossby number.

[1] observed that over a range of scales corresponding to Reynolds numbers (defined precisely below) from $100 < Re < 14000$, over 300 species of birds, bats, insects, and auto-rotating seeds, an associated Rossby number (defined in their paper as the tip radius to chord length ratio) was $Ro = 3$. Owing to morphological constraints, these wings rotate about their root, and in this case, under hovering flight conditions, the Rossby number is also proportional to the

wing's aspect ratio. Note, however, that this is not always the case as the wing root may begin at a distance from the hinge in some species like crane flies. Yet, an obvious question is why $Ro \approx 3$, apart from possible morphological constraints, represents a convergent solution, rather than, say, a smaller value of Ro where Coriolis effects are yet stronger? Again, for wings revolving about their root, detailed analysis of the flow structure revealed an overall loss in coherency of the LEV as the Rossby number increases [1, 11, 12]. Likewise, [13], [10] and [14] showed that for wings undergoing finite amplitude ($< 360°$) revolution there are two distinct flow regions along the wing span: (1) an inboard region where the LEV is stable and generates high lift and (2) an outboard region where the LEV lifts away from the surface, resulting in a local loss in flow coherency. Furthermore, [15] showed that the mean transition between inboard and outboard regions measured for wings undergoing multiple rotations is located approximately four chords away from the axis of rotation.

In this paper we attempt to separate the effects of aspect ratio and Rossby number by varying them independently in the low Reynolds number regime. We perform three-dimensional direct numerical simulations of the flow past an impulsively-started revolving wing at 45° angle of attack. We first examine wings of different aspect ratio revolving about their root, and confirm that lift coefficient is maximized at the aforementioned $Ro \approx 3$ (which coincides with wings of aspect ratio between 3 and 4). We then vary aspect ratio and Rossby number independently by considering wings whose roots are displaced from the center of rotation, and demonstrate that the optimal solution is associated with a compromise between monotonically increasing lift coefficient with aspect ratio, holding Rossby number constant, and monotonically decreasing lift with Rossby number, when holding aspect ratio constant, which is line with some recent observations by [16]. We show that the relative contributions of aspect ratio and Rossby number effects on lift depends on the non-dimensional distance travelled by the wing - i.e. physical mechanisms associated with these parameters have different time scales - and that initial transients have a key role in lift optimality. Specifically, while aspect ratio effects are immediately at play, Ro effects develop with a larger time scale such that large AR wings can produce larger lift for very short distances of travel. However, this occurs for distances of travel corresponding to flapping amplitudes that are not typical of real world observations. As such, we show that wings with AR between 3 and 4 are always optimal in terms of lift production for flapping amplitudes between 70° and 180°, i.e. typical of real world observations. Finally, we provide insights into the physical mechanisms associated with AR and Ro effects. We show that low AR and low Ro limit leading edge vortex growth through downward and spanwise induced velocities, respectively. For sufficiently large damping of the growth rate, the LEV does not interact with the trailing edge, hence avoiding a potential mechanism for vortex shedding [17].

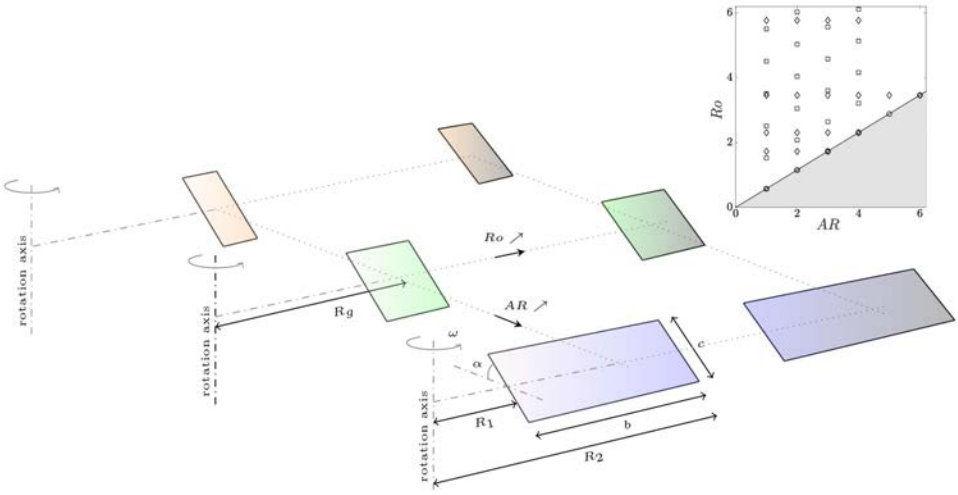

Figure 1: Geometric parameters of the wing and relation with aspect ratio AR and Rossby number Ro. Different colours indicate different AR. Each colour gets darker as Ro increases, i.e. as the wing is displaced from the axis of rotation. The inset shows the cases addressed in this study including constant $R_1 = 0$ ($\circ$), constant AR ($\square$) and constant Ro ($\diamond$) cases.

2 Problem setup

The Navier-Stokes equations are solved for a flat-plate airfoil of rectangular planform using the immersed boundary (IB) and Lattice Green's Function (LGF) method developed by [18, 19]. As depicted in Figure 1, a wing of chord, c, and span, b rotates with angular velocity ω about an axis displaced a distance R_1 from the wing root such that $R_2 = R_1 + b$ is the wing tip. The aspect ratio $AR = b/c$. Following previous work, the Reynolds and Rossby numbers are defined with respect to the wing chord and a characteristic velocity, $V = \omega R_g$, where R_g is the radius of gyration. For a wing of arbitrary planform $R_g^2 = \sqrt{\frac{1}{A}\int_{R_1}^{R_2} r^2 c(r) dr}$, where A is the area, so that for a rectangular wing $R_g = \sqrt{\frac{R_2^3 - R_1^3}{3b}}$. Then $Re = Vc/\nu$ and $Ro = V/(\omega c) = R_g/c$ where ν is the kinematic viscosity of the fluid. In this paper, cases with $AR \in [1 - 7]$ and $Ro \in [0.58 - 6.03]$ are addressed. Note that $Ro = 0.58$ is the lowest possible Rossby number for the range of AR tested. Also note that the definition of Ro differs from that used by [1] where the tip radius rather than the radius of gyration was used, such that Ro was equal to AR for wings with root located on the axis of rotation ($R_1 = 0$). Re is set to 577, which corresponds to a Reynolds number based on the mean wing speed across the span of 500 for wings with $R_1 = 0$ (i.e. comparable to cases addressed in [4, 5]), and within the range of Reynolds numbers considered by [1]. The lift coefficient is defined

as $C_L = L/\frac{1}{2}\rho V^2 A$, where L is the lift of the wing (force parallel to the axis of rotation) and ρ is the density of the fluid.

The IB-LGF method discretizes the incompressible Navier-Stokes equations on a formally unbounded (infinite) staggered Cartesian grid using a second-order finite-volume scheme [18]. The system of differential algebraic equations resulting from the spatial-discretization of the momentum equation and the incompressibility constraint are integrated in time by using an integrating factor technique for the viscous terms and a specialized half-explicit Runge-Kutta scheme for the convective term and the incompressibility constraint. The flow is solved using only information contained in the finite grid region where the vorticity and the divergence of the Lamb vector have non-negligible support. An adaptive block-structured grid and a velocity refresh technique are used to limit operations to a relatively snug finite computational domain surrounding the wing. The flow is solved in a frame of reference accelerating with the immersed wing. The IB treatment is similar to the original approach of [20] and based on the discrete delta function of [21]. The projection approach of [22] is utilized to determine the surface forces that identically yield a slip-free condition for the velocity field interpolated onto a set of quadrature points that define the immersed surface. In our case, the grid resolution and immersed boundary point spacing are set to $\Delta s = 0.015c$. Grid convergence tests were performed for a reference case ($R_1 = 0$, $AR = 4$) and showed that the mean lift coefficient obtained using the reported spatial resolution is only 1.7% away from the Richardson-extrapolated solution [23]. To ensure time accuracy, the time step is chosen to ensure that the Courant number (CFL) does not exceed 0.5.

Figure 2 compares the three-dimensional flow field obtained for this reference case with results obtained by [24] at a higher, yet low Reynolds number ($Re \approx 3000$). Q-criterion isosurfaces are used, with iso-values equal to 0.9 in both cases (non-dimensionalized using the wing chord and the velocity at the radius of gyration). Very good agreement is observed, although experimental flow fields exhibit smaller scale structures that arise from Reynolds number effect and measurement noise. In addition, we reproduce simulations by [25], where $R_1 = 0.52c$, $AR = 1$ and $Re = 520$. Figure 3 compares the mean lift and drag coefficients (averaged over $\phi \in [45^\circ - 315^\circ]$) obtained using the present approach with those obtained by [25]. Here again, good agreement is observed despite slight discrepancies that may arise from slightly different setup; i.e. [25] considered a non-zero thickness wing with a different acceleration program. Note that non-dimensional values reported in [24] and [25] have here been recalculated with respect to the wing chord and the wing velocity at the radius of gyration.

In what follows, we consider an angle of attack of 45° and an impulsively-started rotation (step function) through 180° of rotation to simulate the half-stroke of a hovering, flapping wing. This amplitude of rotation encompasses that observed in nature (typically between 70 and 180°) [26]. and somehow consitutes an upper anatomical limit. This setup allows to investigate the quasi-steady state of the flow, as is commonly achieved in revolving wing studies. In addition, it further allows to extract the fundamental role of initial transients

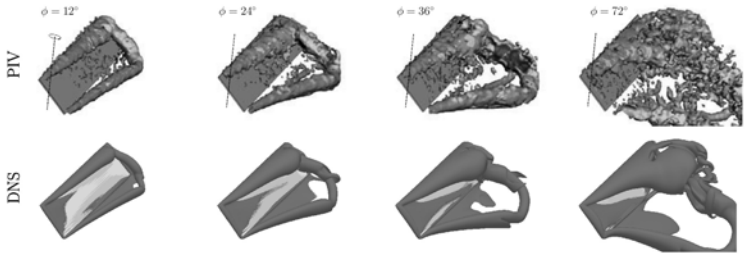

Figure 2: Comparison of Q-criterion isosurfaces obtained experimentally (stereoscopic Particle Image Velocimetry - PIV - measurements) by [24] with those obtained using the present numerical approach (DNS). The iso-value of the Q-criterion (non-dimensionalized using the wing chord and the velocity at the radius of gyration) is set to 0.9 in both numerical and experimental cases.

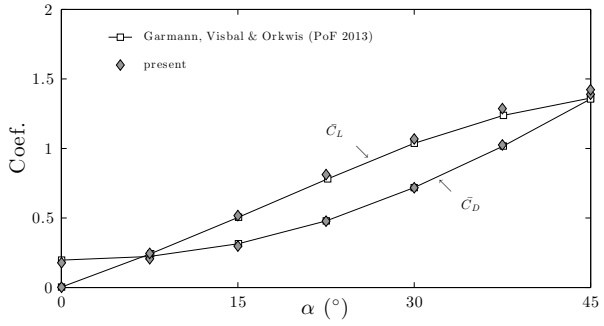

Figure 3: Comparison of mean lift and drag coefficients obtained by [25] with those obtained using the present approach.

on the three-dimensional mechanisms that drive lift generation by discarding any dependency to flapping wing kinematics (which considerably reduces the parameter space of the problem). It is stressed that because only a simple rotation is considered, additional mechanisms pertaining to flapping flight (such as wake capture) are not taken into account. Caution must therefore be exercised in drawing implications for flapping flight, as is discussed more fully in section 3 3.4.

The flow is analyzed in terms of Q-criterion [27] isosurfaces at the end of the revolving motion ($\phi = 180°$) where the flow has reached a quasi-steady state. Cross-sectional vorticity and spanwise velocity contours are also shown at different instants. These quantities are correlated with lift generation. In what follows, unless otherwise specified, all data are non-dimensionalized with respect to the wing chord and the wing velocity at the radius of gyration.

3 Results

3.1 Wings revolving about their root

We first consider different aspect ratio wings with $R_1 = 0$. Figure 4a shows the mean lift coefficient $\bar{C_L}$ (averaged over the first 180° of revolution) obtained for aspect ratios ranging from 1 to 7. An optimal lift coefficient is obtained for an aspect ratio between 3 and 4, which correlates well with the aspect ratio of hummingbird wings (on the order of 3.7) and that of other species [26, 1]. Figures 4b and 4c show Q-criterion [27] iso-surfaces obtained for each case at the end of the revolving motion ($\phi = 180°$). For sufficiently high aspect ratios ($AR > 4$), it is observed that a conical LEV develops on the upper surface of the wing and extends from the wing root to approximately 3 chords away from it. Further outboard of the wing, the flow is characterized by smaller scale unsteady vortices that indicate local flow instability. This distinction between inboard quasi-steady flow and outboard unsteady flow reflects local Rossby number (r/c) effects and the enhanced role of Coriolis effects on flow stability as r decreases [1]. The extent of the quasi-steady inboard region where the LEV is found to be robustly attached is consistent with data obtained by [15] on wings undergoing multiple rotations. Overall, it can be speculated from these results that increasing aspect ratio beyond 4 is detrimental (as seen in figure 4(a)) because of the instability that occurs in the outboard region of the wing. For lower aspect ratios ($AR < 4$), the tip condition influences the inboard quasi-steady region such that the conical LEV reorients along the chord as it merges with the tip vortex (TV), at a position $r/c < 3$ (e.g. see inset of $AR = 2$ case in figure 4b).

Figure 5a shows the evolution of the lift coefficient C_L as a function of the revolution angle ϕ for all cases. Occurrence of flow instability in the outboard region can be correlated with a rapid drop in lift for cases with $AR > 4$. Naturally, the drop in lift does not occur at similar instants for cases with $AR = 5$, 6 and 7 because the distance traveled by the wing at a given ϕ scales with $\phi \times R_g$

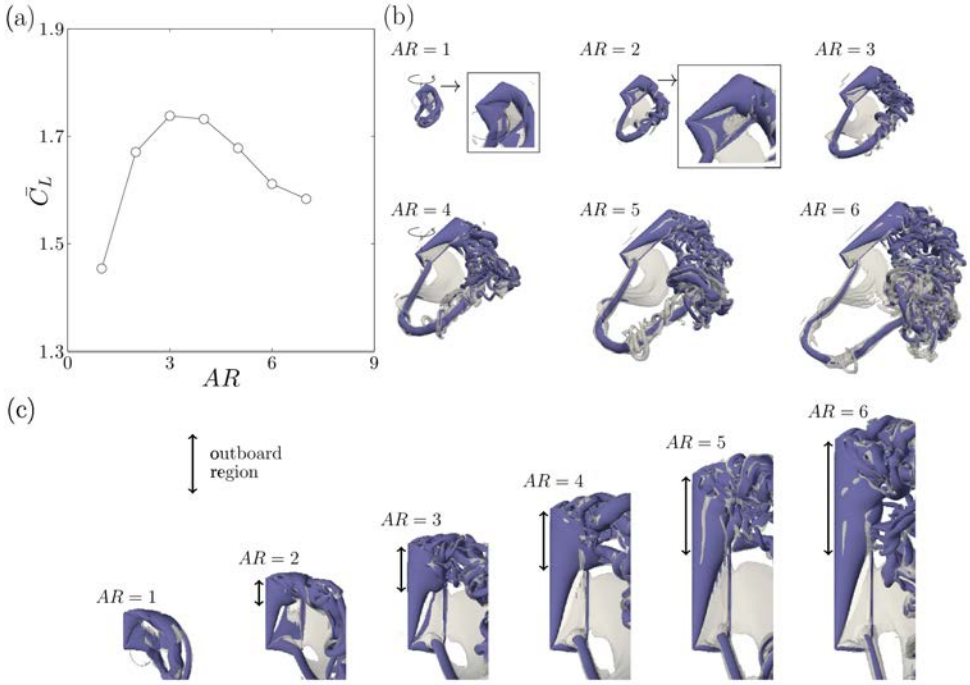

Figure 4: (a) Mean lift coefficient obtained for wings with aspect ratio $AR \in [1-7]$ and constant root location $R_1 = 0$. (b) Perspective and (c) back view of Q-criterion isosurfaces (iso-values 0.01 and 1 are displayed in light grey and blue respectively) obtained at $\phi = 180°$ for $AR \in [1-6]$.

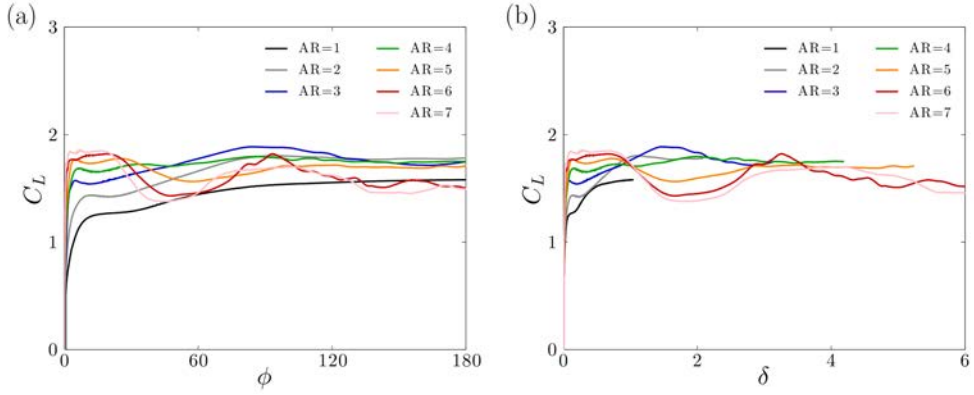

Figure 5: Instantaneous lift coefficient as a function of (a) the revolution angle ϕ and (b) non-dimensional distance travelled by the wing at the radius of gyration δ, obtained for wings with aspect ratio $AR \in [1-7]$ at constant root location $R_1 = 0$.

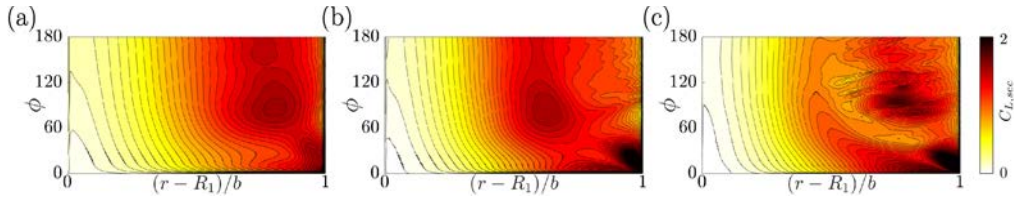

Figure 6: Isolines and contours of instantaneous sectionnal lift coefficient $C_{L,sec}$ as a function of the revolution angle ϕ and the position along the span $(r-R_1)/b$ obtained for wings with aspect ratio (a) $AR = 2$, (b) 4 and (c) 6 at constant root location $R_1 = 0$.

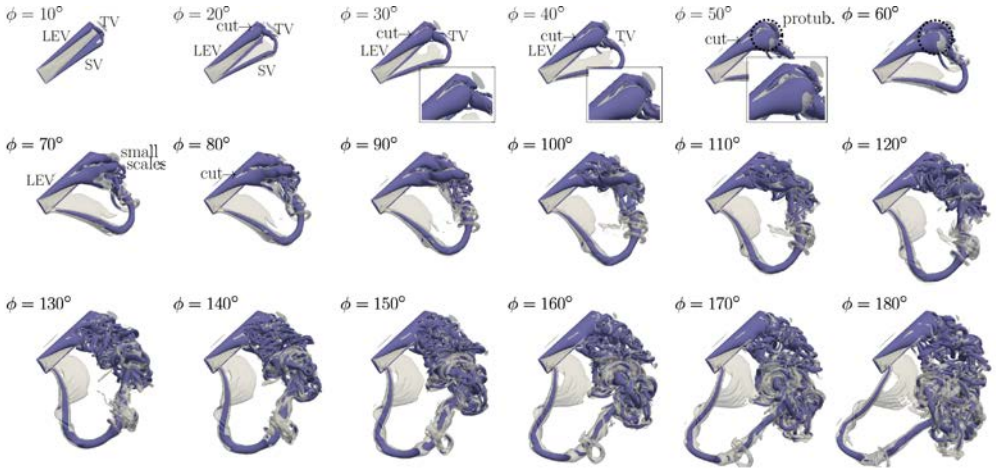

Figure 7: Q-criterion isosurfaces (iso-values 0.01 and 1 are displayed in light grey and blue respectively) obtained every $\phi = 10°$ for the $AR = 6$ case. The time-sequence shows the development of outboard flow unsteadiness characterized by small scale structures for $r/c > 3$, as opposed to the quasi-steady inboard flow characterized by a stable LEV for $r/c < 3$.

(or any arbitrary radial length of reference), and R_g increases with AR. That is, lift drop occurs more quickly for higher values of AR. Plotting the evolution of C_L as a function of the non-dimensional distance traveled by the wing at the radius of gyration $\delta = \phi R_g/c$, or convective time at the radius of gyration, in figure 5b shows that the instant of lift drop for $AR > 4$ better matches, suggesting that flow instability in the outboard region of the wing scales with δ. This point will be further addressed in section 33.4.

The footprint of outboard flow instability on lift can also be clearly visualized by mapping contours of sectional lift coefficient $C_{L,sec}$ as a function of $(r-R_1)/b$ and ϕ in figure 6. For $AR = 6$, it can be seen that iso-lines have a preferential orientation along the vertical direction from root to mispan (i.e. in the $r/c < 3$ region). This indicates that $C_{L,sec}$ (1) increases with r and (2) saturates as ϕ tends to 180°. Such a trend is typical of a conical LEV reaching a steady state. On the contrary, iso-lines beyond midspan (i.e. in the $r/c > 3$ region) do not have a preferential orientation. This indicates both time-fluctuations and non-monotonic spanwise variations in $C_{L,sec}$, which is indicative of vortex shedding and loss in coherency in the outboard region. For $AR = 4$, this outboard unsteadiness and loss in coherency occurs over a much smaller proportion of the wing. Therefore, the drop in $C_{L,sec}$ does not have a significant impact on the global lift coefficient C_L. For $AR = 2$, there is no clear evidence of any flow instability inducing significant temporal fluctuations in $C_{L,sec}$. Correspondingly, the C_L versus ϕ curve is roughly constant.

Figure 7 provides further evidence of the occurence of outboard flow unsteadiness with time. The time sequence shows Q-criterion isosurfaces obtained for $AR = 6$ ($R_1 = 0$) every 10° of rotation. At $\phi = 10°$, the flow exhibits smooth leading, trailing (or starting) and tip vortices (LEV, SV and TV respectively). The SV is rapidly shed into the wake while being connected with the TV. The LEV initially develops close to the wing surface but is also found to rapidly detach from the leading edge in the outboard region, as indicated by the cut in the outboard Q-criterion isosurfaces at $\phi = 20°$. This cut then propagates towards the wing midspan as ϕ increases, together with a global increase in the size of the outboard LEV. At some point, the outboard LEV that merges with the TV forms an outboard protuberance ($\phi = 50°$ and 60°) that eventually bursts into small scale structures ($\phi = 70°$) [28]. For $\phi > 70°$, there are no clear changes in the spanwise position of the cut in Q-criterion isosurfaces, which corresponds to the frontier between quasi-steady inboard and unsteady outboard region. It can be observed that while the inboard flow exhibits a smooth conical LEV, it is characterized in the outboard region by fluctuating small scale structures without any preferential orientation.

3.2 Aspect ratio variation with constant Rossby number

We now consider wings of different aspect ratios at constant Rossby number. Physically this is achieved by displacing the wing root from the axis of rotation in inverse proportion to the aspect ratio. Figure 8(a) shows the mean lift coefficient $\bar{C_L}$ obtained for aspect ratios ranging from 1 to 6 at Rossby numbers of 1.73, 2.31, 3.46 and 5.77. It is shown that lift monotonically increases with AR for all Rossby numbers. In particular, the increase is relatively strong for low AR and follows an asymptotic trend for larger AR. This trend is qualitatively similar to that observed by [3] for translating wings ($Ro \to \infty$) at low Re, where it was also pointed out that the trends were qualitatively similar to predictions from the three-dimensional potential flow (inviscid) theory [29, 30]. Because at high angle of attack, in the separated flow regime, the total aerodynamic force principally acts in a direction normal to the wing surface, the dependence of drag on wing parameters is similar to that of lift. A figure showing the mean drag coefficient as a function of AR is provided as supplementary material, figure A. Figure 8b shows Q-criterion isosurfaces obtained for cases with Rossby number 3.46 at the end of the revolving motion ($\phi = 180°$). As AR decreases, the outboard unsteady region appears to be truncated (in that its spanwise extent is reduced) while the inboard quasi-steady region exhibits an increase in LEV conicity. Here again, the transition from quasi-steady to unsteady regions is found to occur around three chord from the axis of rotation for $AR > 1$, which supports the idea that LEV stability is driven by r/c, i.e. the local Rossby number. In the $AR = 1$ case, the proximity between root and tip vortices tend to damp outboard unsteadiness such that both root and tip vortices exhibit relatively smooth shape, as opposed to higher AR cases where the tip vortex comprises multiple smaller scale structures.

The increased effect of root and tip vortices in the $AR = 1$ case can also be

observed by comparing cross-sectional contours of spanwise vorticity obtained at the radius of gyration for cases with $AR = 1$, 2 and 4 and $Ro = 3.46$. Snapshots are shown in figure 9 for four values of $\delta = 0.5$, 1, 1.5 and 2, corresponding to the build-up and shedding phases of the intial LEV. At $\delta = 0.5$, all cases exhibit relatively similar patterns with leading edge and trailing edge vorticity sheets that roll up into leading edge and trailing edge vortices, respectively. While the trailing edge vortex, or starting vortex (SV), is rapidly shed, the LEV develops close to the wing surface. At $\delta = 1$, for $AR = 2$ and 4, the LEV in turn sheds into the wake. LEV shedding is promoted by the eruption of opposite sign vorticity from the wing upper surface, that tends to cut the feeding leading edge shear layer [17]. Conversely, although the bottleneck in the leading edge shear layer of the $AR = 1$ case suggests imminent shedding (in that a bottleneck generally precedes a cut in Q-criterion isolines, which we assume to be representative of vortex shedding), the LEV remains attached to the wing due to downward induced velocity from root and tip vortices. Snapshots at $\delta = 1.5$ show a clear offset between the position of the attached LEV for $AR = 1$ and that of the shed LEV that advects downstream for $AR = 2$ and 4. The induced downwash is further reflected by the nearly horizontal leading edge shear layer in the $AR = 1$ case, as opposed to an inclined shear layer in the $AR = 2$ and 4 cases, which indicates that the wing operates at a lower effective incidence. Overall, the induced downwash and its increased relative importance on the global flow structure as the aspect ratio decreases result in reduced lift, which explains the trend observed on figure 8a. In addition to the induced downwash, it is important to note that favorable spanwise flow may also play a role on the LEV attachment observed in the $AR = 1$ case, specifically at low Ro. This point is discussed in the next section.

3.3 Rossby number variation at fixed aspect ratio

Finally, we consider wings at different Rossby numbers and constant aspect ratio. Figure 10a shows the mean lift coefficient $\bar{C_L}$ obtained for Rossby numbers ranging from 0.58 to 6.03 and aspect ratio 1, 2, 3 and 4. Here again, it is demonstrated that lift evolves monotonically with Ro for all ARs. In particular, $\bar{C_L}$ is found to increase roughly linearly as Ro decreases within the range of Ro considered, with a slope that appears to be roughly independent of AR. Similar results are obtained for the drag coefficient (see figure B provided as supplementray material). Figure 10b shows Q-criterion isosurfaces obtained for cases with aspect ratio 2 at the end of the revolving motion ($\phi = 180°$). As previously found by [1] and [11], it can be seen that the flow loses coherency as Ro increases from 1.15 to 3.06. That is, the outboard unsteady region gains relative importance along the span with respect to the inboard region as Ro increases. Further evidence of this is provided in figure 11 where contours of sectional lift coefficient $C_{L,sec}$ are mapped as a function of $(r - R_1)/b$ and ϕ for $AR = 2$ and $Ro = 1.15$, 2.08 and 3.06. It is shown that as Ro increases, vertical iso-lines inboard reorients along arbitrary directions, indicating the occurence of time-fluctuations and non-monotonic spanwise variations in $C_{L,sec}$, i.e. vortex

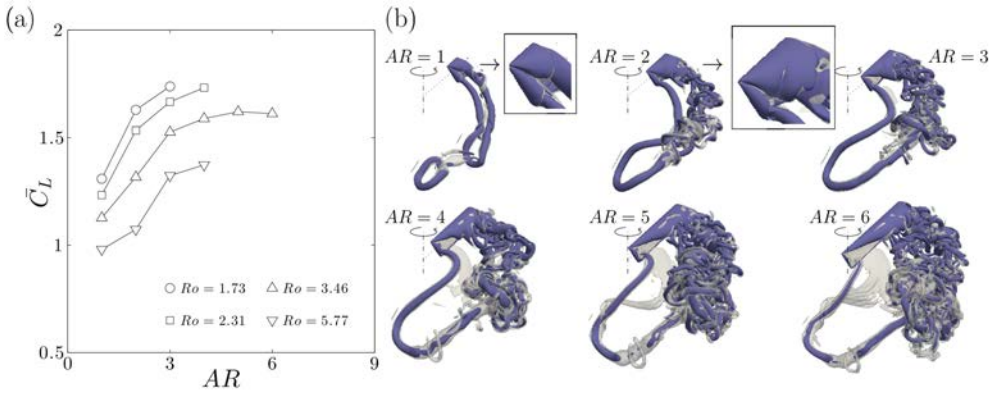

Figure 8: (a) Mean lift coefficient for wings with aspect ratios $AR \in [1-6]$ and constant Rossby numbers $Ro = 1.73$, 2.31, 3.46 and 5.77. (b) Q-criterion iso-surfaces (iso-values 0.01 and 1 are displayed in light grey and blue respectively) obtained at $\phi = 180°$ for $Ro = 3.46$ cases.

shedding and loss in coherency. As Ro is further increased, changes in the flow structure are less striking (figure 10b). Rather, the quasi-steady flow observed inboard results from root vortex (RV) effects, in a similar way to what can be observed for translating wings. These effects do not change much as Ro increases, although the asymetry between root and tip vortices decreases.

Figures 12 and 13 show cross-sectional contours of spanwise vorticity and spanwise velocity obtained at the radius of gyration for cases with $Ro = 1.15$, 2.08 and 3.06 and $AR = 2$. Again, snapshots are displayed at $\delta = 0.5$, 1 and 1.5, which is representative of the build-up and shedding phases of the intial LEV. First, figure 12 clearly indicates that a lower Rossby number is conducive to LEV attachment. In particular, while evidence of LEV shedding can be observed at $\delta = 1$ for $Ro = 3.06$, it is postponed to $\delta = 1.5$ for $Ro = 2.08$ and absent for $Ro = 1.15$. For $Ro = 1.15$, there is no striking changes between the LEV structure at $\delta = 1$ and that at $\delta = 1.5$, which is consistent with the nearly constant lift observed on figure 5 and the corresponding maps of instantaneous lift shown in figure 11a. This is also in line with recent results on flapping and revolving wings (obtained by [31] and [32], respectively) where increased LEV growth rate, quicker vortex shedding and lower lift were observed with increasing Ro. Second, it can be seen from figure 13 that LEV attachment is highly correlated with the development of spanwise flow. Present results show that a lower Rossby number is conducive to the development of outboard flow in the core and behind the LEV. Spanwise flow was also observed to increase with reduced Rossby numbers by [11].

Spanwise flow due to lower Rossby numbers do not appear immediately but still rather early in the motion (note that $\delta = 0.5$ corresponds to $\phi = 25°$ when $Ro = 1.15$). This spanwise flow adds to that arising from spanwise gradients

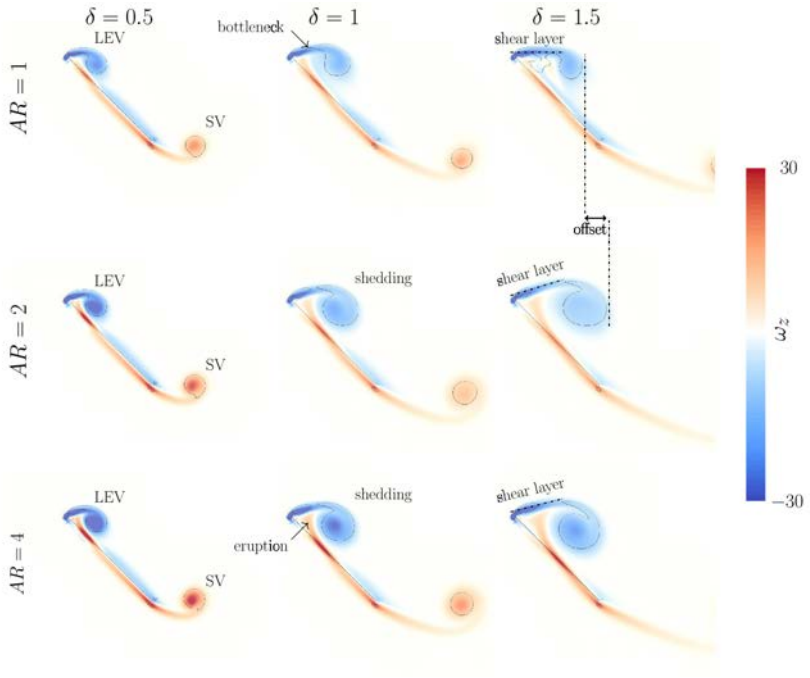

Figure 9: Cross-sectional spanwise vorticity contours obtained at the radius of gyration at $\delta = 0.5$, 1 and 1.5. Cases with $Ro = 3.46$ and $AR = 1$, 2 and 4 (from top to bottom) are displayed. LEV shedding is observed for $AR = 2$ and 4 but not for $AR = 1$ where the effective angle of attack is reduced.

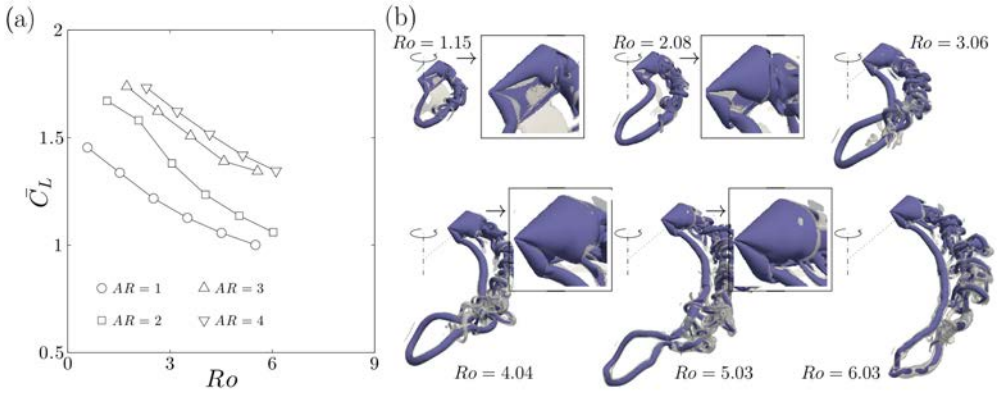

Figure 10: (a) Mean lift coefficient for wings with Rossby numbers $Ro \in [0.58 - 6.03]$ and constant aspect ratio $AR = 1$, 2, 3 and 4. (b) Q-criterion isosurfaces (iso-values 0.01 and 1 are displayed in light grey and blue respectively) obtained at $\phi = 180°$ for the $AR = 2$ cases.

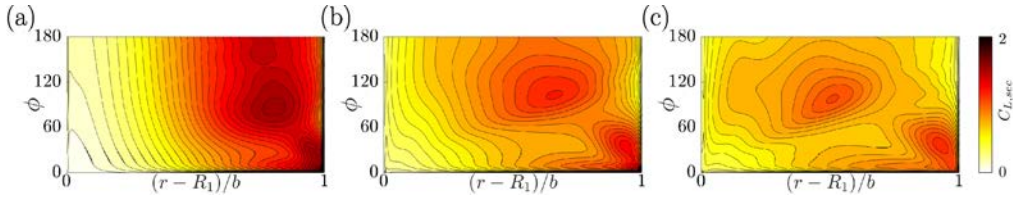

Figure 11: Isolines and contours of instantaneous sectionnal lift coefficient $C_{L,sec}$ as a function of the revolution angle ϕ and the position along the span $(r-R_1)/b$ obtained for wings with aspect ratio $AR = 2$ and Rossby numbers (a) $Ro = 1.15$, (b) 2.08 and (c) 3.06.

in flow speed [4], hence spanwise gradients in LEV circulation, which develops independently to the Rossby number. Indeed, although spanwise gradients in flow speed are inherent to revolving motion (the velocity in the non-inertial frame of reference is higher at the wing tip than at the wing root), they are related to the presence of spanwise shear and thus occur in any type of shear flows without rotational effects. The combination of spanwise flows arising from rotational effects and spanwise gradients in flow speed contributes to spanwise vorticity drainage, which helps balance vorticity production at the leading edge (also see some recent analytical model by [7] on this matter).

To further quantify spanwise vorticity drainage, we perform a vorticity transport analysis similar to that described in [33]. The analysis is performed on a control surface defined by the intersection of a closed vorticity isocontour and vertical lines located at the leading and trailing edges. The value of the vor-

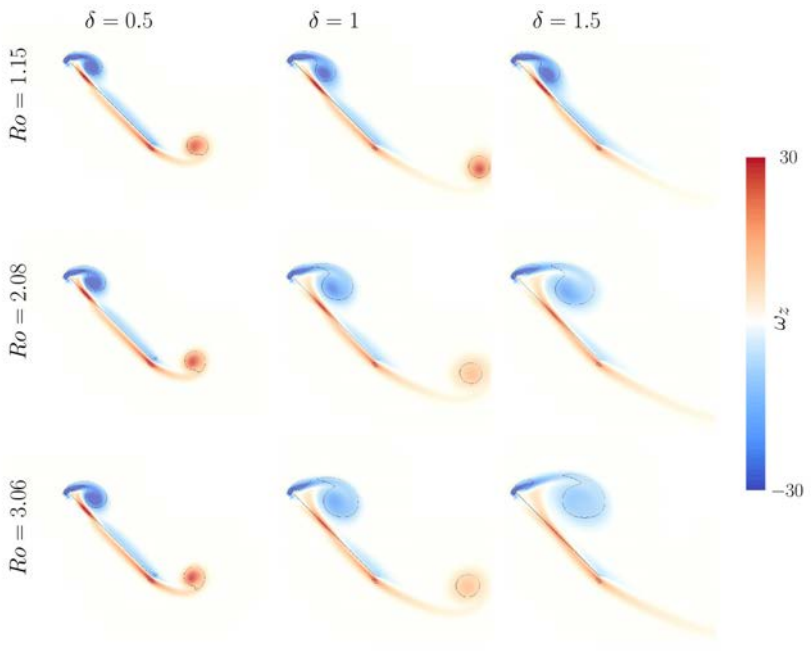

Figure 12: Cross-sectional spanwise vorticity contours obtained at the radius of gyration at $\delta = 0.5$, 1 and 1.5. Cases with $AR = 2$ and $Ro = 1.15$, 2.08 and 3.06 (from top to bottom) are displayed.

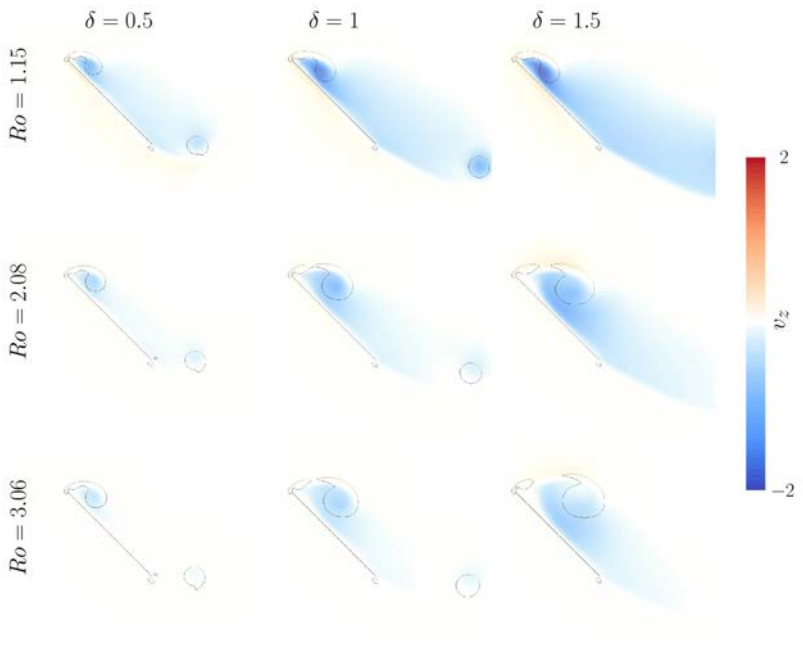

Figure 13: Cross-sectional spanwise velocity contours obtained at the radius of gyration at $\delta = 0.5$, 1 and 1.5. Cases with $AR = 2$ and $Ro = 1.15$, 2.08 and 3.06 (from top to bottom) are displayed.

ticity isocontour is set to -0.1, which is approximately 1% of the peak vorticity value in the control surface. In our low Reynolds number cases, there is no clear distinction between the LEV and the aft vorticity layer in terms of vorticity levels. This is contrary to higher Reynolds number cases [33] where the LEV is more compact and can thus be isolated from the aft vorticity layer with a reasonably low value of vorticity isocontour. Figure 14a shows an example of the control surface used, together with vorticity fluxes. Here, $f_{x,i} = \int_{L_i} v_x \omega_z dy$ and $f_{x,o} = \int_{L_o} v_x \omega_z dy$ are the chordwise fluxes of vorticity through the leading and trailing edge lines, L_i and L_o, respectively. $f_{x,i}$ feeds vorticity inside the control surface whereas $f_{x,o}$ contributes to chordwise drainage. The resulting chorwise flux is $f_x = f_{x,i} + f_{x,o}$. $f_z = \int_S v_z \partial \omega_z / \partial z dx dy$ is the spanwise flux through the control surface S.

Figure 14b shows the f_z/f_x ratio computed in a chordwise cross section located 1/4 span away from the wing root (i.e. at $r = R_1 + b/4$) for the three cases $AR = 2$ and $Ro = 1.15$, 2.08 and 3.06. The 1/4 span location is chosen to allow better comparison with the previous analysis by [33] and to ensure sufficient distance to the wing tip to reduce any potential tip effects on spanwise flow. It can be seen that for all cases the f_z/f_x ratio increases during the initial stages of the motion, yet with different growth rates. The growth rate is the highest for the lowest Rossby number $Ro = 1.15$, where the f_z/f_x ratio reaches values on the order of 0.6 near $\delta = 0.5$ and then remains at sustained levels. In the $Ro = 2.08$ case, f_z/f_x rapidly stops increasing to oscillate in the range $0.2 - 0.3$, and eventually decreases monotonically for $\delta > 1$. In the $Ro = 3.06$ case, f_z/f_x rapidly drops and even changes sign near $\delta = 0.6$. Overall, these results corroborate the fact that outboard spanwise vorticity drainage is enhanced as the Rossby number decreases. The sustained value of f_z/f_x correlates well with the attached LEV in the $Ro = 1.15$ case whereas the rapid drop in f_z/f_x correlates well with LEV shedding in the $Ro = 3.06$ case; the $Ro = 2.08$ being an intermediary case where LEV attachment is postponed with respect to higher Rossby number cases. However, it can also be noted that outboard drainage cannot, in its own, balance streamwise fluxes. This is line with previous results by [33] who suggested that vorticity annihilation due to the interaction between the LEV and the opposite sign vorticity layer on the wing surface could play an important role in vorticity regulation inside the control surface. In addition, although not shown here for the sake of conciseness, our results suggest that in these low Reynolds number cases a non negligible amount of vorticity is advected through the aft vorticity layer to the wake, resulting in a $f_{x,o}/f_{x,i}$ ratio that rapidly increases to 0.1 for all cases. While different mechanisms may exist to regulate vorticity inside the control surface, it is here shown that lower Rossby numbers are conducive to spanwise vorticity drainage and thus contributes to limiting LEV growth. If the growth rate is sufficiently reduced, the LEV will not interact with the trailing edge, hence avoiding a potential mechanism for vortex shedding [17].

Finally, the control surface displayed in figure 14a can be used to estimate the Coriolis force acting on it. In the non-inertial reference frame of reference,

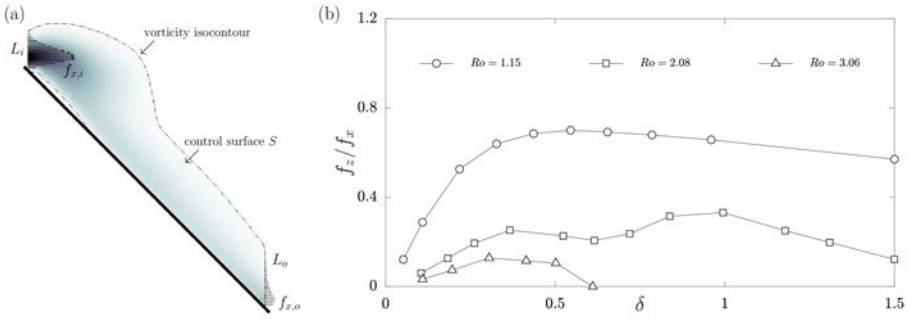

Figure 14: (a) Representative control surface for the vorticity transport analysis. (b) Ratio of spanwise to chordwise vorticity fluxes through the control surface at $r = R_1 + b/4$ for $AR = 2$ and Rossby numbers $Ro = 1.15$, 2.08 and 3.06.

a fluid particle in still air experiences an inboard Coriolis force with magnitude $2\rho\omega r^2$. If a revolving wing is introduced, this inboard force will be reduced because the azimuthal component of the velocity in the non-inertial frame of reference will be reduced (the velocity of the wing in this reference frame is zero) [8]. Note that the centrifugal force won't change because it does not depend on the fluid velocity. Therefore, a fluid particle will experience an outboard force with respect to that in still air, with magnitude $2\rho\omega u'_\theta$ (where u'_θ is the azimuthal component of the fluid velocity perturbation with respect to the still air case). Integrating $2\rho\omega u'_\theta$ over the control surface shows that the outboard force coefficient $\int_S 2\omega u'_\theta dxdy/c(\omega r)^2$ (i.e. non-dimensionalized using the local wing velocity at a quarter span) decreases with Ro. For instance, values of 0.21, 0.12 and 0.07 are obtained at $\delta = 0.5$ for $Ro = 1.15$, 2.08 and 3.06 respectively.

3.4 Discussion

While an aspect ratio between 3 and 4 maximizes lift on a wing undergoing a 180° rotation about its root, this does not necessarily imply that the same is true for a flapping wing. In particular, flapping wings with high aspect-ratio ($AR > 4$), for which LEV shedding is observed outboard, could adopt kinematics such that pronation/supination occurs prior to LEV shedding, hence avoiding the associated drop in lift. Nevertheless, figure 5 suggests that, for $AR > 4$, the flapping amplitude should be reduced to approximately 30° to avoid such a drop. As pronation and supination phases are known to be detrimental to the overall production of lift, because the rotational speed decreases to zero during stroke reversal, the time over which they occur should be minimized with respect to the flapping period. This means that for a given time of pronation/supination (and fixed wing speed, or Reynolds number), flapping amplitude should be maximized. This was shown by [34]. It therefore appears

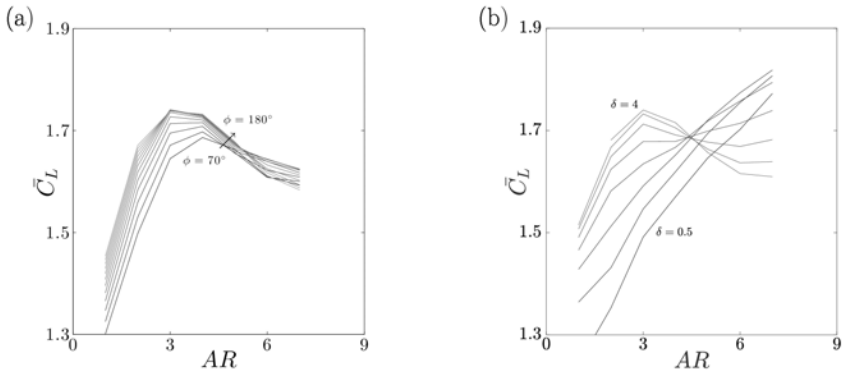

Figure 15: Influence of the amplitude of rotation on the mean lift coefficient obtained for wings with aspect ratio $AR \in [1 - 7]$ and constant root location $R_1 = 0$. Results are shown in terms of revolution angle ϕ (a) and non-dimensional distance travelled by the wing at the radius of gyration δ (b).

that reducing the flapping amplitude such that LEV shedding does not occur during the revolving phase of an aspect ratio $AR > 4$ flapping wing would not compensate for the loss in lift, because pronation and supination phases would encompass a greater percentage of the flapping period. And this despite the fact that effects such as wake capture can mitigate the lift decrement due to decreasing rotational speed. Figure 15a replicates figure 6 for lower amplitudes of rotation ϕ. Amplitudes tested are withing the range [70°-180°] (10° step), which encompasses flapping amplitudes of most insects [26]. It is striking that for all amplitudes, the lift-optimal aspect ratio is always between 3 and 4. In other words, the lift optimal aspect ratio of a revolving wing appears to be roughly independent of the amplitude of rotation within the range observed in nature. In addition, around the optimal aspect ratio, curves collapse as the amplitude increases, which indicates that for such low aspect ratio the flow reaches a quasi-steady state.

We emphasize that the mean lift is obtained by averaging the instantenous lift from the impulsive start, i.e. $\phi = 0°$, thereby taking into account initial transients. It can be observed from figure 5 that averaging once intital transients have decayed would not reveal a clear lift optimum because the lift coefficients of $AR = 2$, 3 and 4 cases converge towards similar values. This may partly explain why studies on rotating wings [15] cannot reveal a clear optimal lift.

Therefore, although early studies suggested this (but in a different, two-dimensional framework where physical mechanisms are different), we insist on the fact that initial transients have a key role in lift generation on revolving and flapping wings. Mechanisms such as the development of spanwise flow, the development of root and tip vortices and the production of vorticity at the leading edge have competing time scales that eventually drive the development of the

LEV during intial transients, hence the lift force. A model of lift generation on flapping wings has to take into account these competing time scales. In this regard, as previously addressed in section 33.1, the thorough analysis of AR and Ro effects on revolving wings should be achieved keeping the non-dimensional distance travelled by the wing constant. This is true in the post-transients phase (unless all lift coefficients reach a quasi-steady state) but it is even more crucial when initial transients are taken into account. Again, when comparison is made between different cases keeping the revolving amplitude constant, the distance travelled by the wing increases with AR or Ro. Therefore, mean coefficients computed at fixed AR or Ro include effects of variation in non-dimensional distance of travel. For the sake of completeness, we averaged lift over constant δ (computed at the radius of gyration) rather than constant revolving amplitude ϕ and plotted it as a function of the aspect ratio for cases with constant root location on figure 15b. Values of δ are within the range $[0.5 - 4]$ (with step of 0.5). It is shown that the lift increases monotonically with AR for low values of δ whereas it peaks for an aspect ratio between 3 and 4 for larger values. In the range $\delta \in [0.5 - 2.5]$, higher aspect ratio cases still benefit from initial transients and the impact of vortex stabilization (through rotational acceleration) on lift is not yet effective. Figure 5 shows that during initial transients, lift increases monotonically with AR. However, as δ increases beyond 2.5, Ro effects counteract AR effects and an optimal lift is observed for an aspect ratio between 3 and 4. Note that the above limit $\delta = 2.5$ corresponds to amplitude ϕ below 70° for $AR \geq 4$ cases, i.e. below typical amplitudes observed in nature [26]. Transient effects are further highlighted on figures 16a and b where the lift coefficients at constant Ro and constant AR are averaged over 2 chords of travel. It is striking that the constant Ro curves on figure 16a collapse, indicating the weak dependence of lift on rotational effects during initial transients. This trend can also be observed on figure 16b where constant AR curves are roughly horizontal for sufficiently large values of Ro. Yet, one can still observe the impact of rotational effects for low values of Ro. The threshold at which constant AR curves diverge from a horizontal line is found to be around 3, again echoing observations by [1]. These constant Ro and AR curves converge towards those obtained in figures 8a and 10b if the distance of travel over which the lift is averaged increases. This is illustrated in figures 17a and b where the lift coefficients are averaged over 10 chords of travel. In some way, this can be viewed as rotational effects propagating radially outboard from the wing root, again highlighting the role of the local Rossby number r/c. This propagation and the importance of local Rossby number can further be observed on figure 18 which shows cross-sectional contours of spanwise velocity $v_{z,loc}$ obtained in the $AR = 6$, $R_1 = 0$ case at different radial locations r/c. Contours are displayed for 3 values of non-dimensional distance of travel δ_{loc}. Note that spanwise velocity and distance of travel are here non-dimenzionalized using the local wing speed at the corresponding r/c location (noted with subscript $_{loc}$). It is evident from figure 18 that LEV growth rate decreases and spanwise velocity increases with both decreasing r/c and increasing δ_{loc}.

Overall, it can be seen that AR effects always have a strong impact on lift

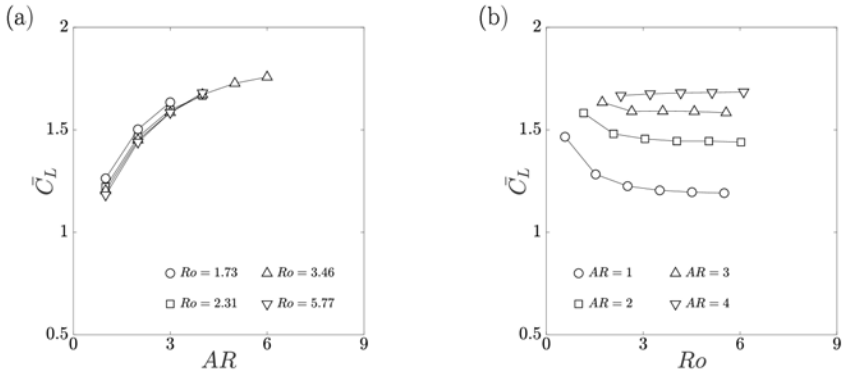

Figure 16: Lift coefficients averaged over 2 chords of travel for constant Ro (a) and constant AR (b) wings.

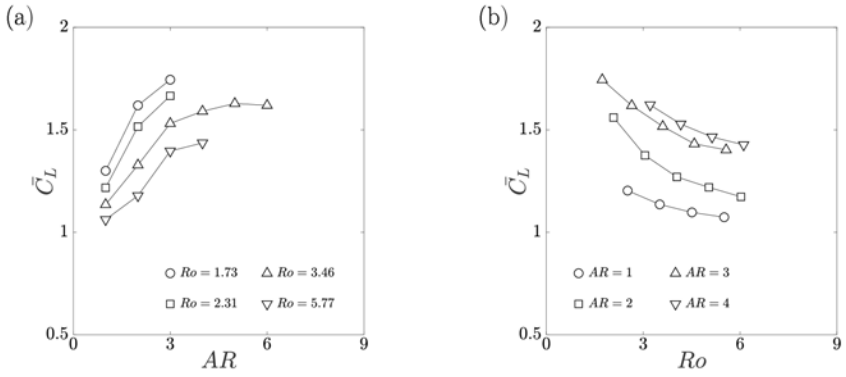

Figure 17: Lift coefficients averaged over 10 chords of travel for constant Ro (a) and constant AR (b) wings.

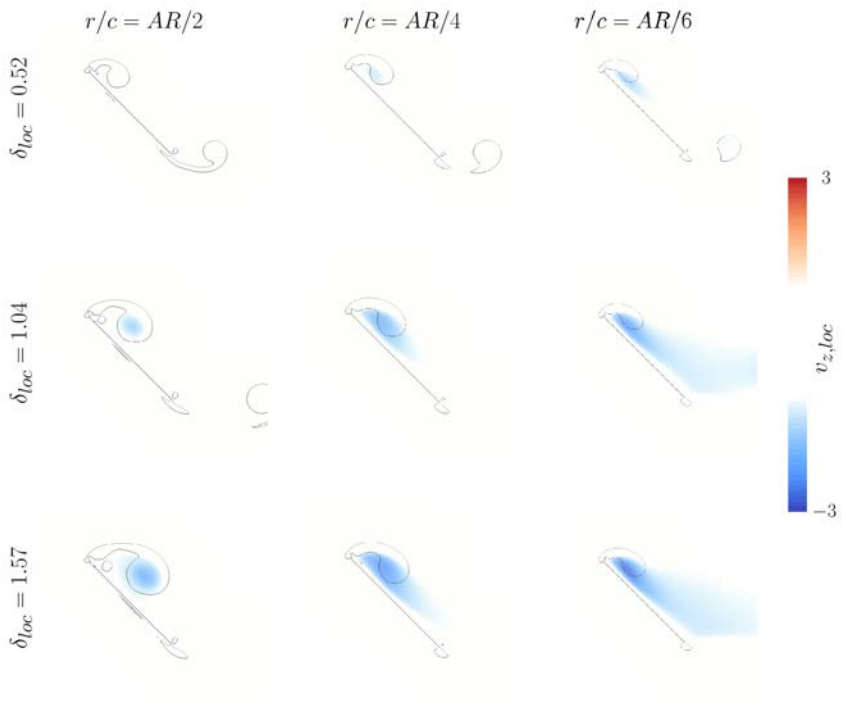

Figure 18: Cross-sectional spanwise velocity contours obtained at 1/2, 1/4 and 1/6 span of the $AR = 6$ and $R_1 = 0$ case. Non-dimensionalized local distances of travel $\delta_{loc} = 0.52$, 1.04 and 1.57 (from top to bottom) are displayed.

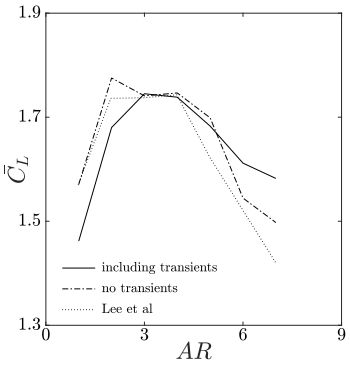

Figure 19: Mean lift coefficient obtained for wings with aspect ratio $AR \in [1-7]$. Mean values are obtained including (plain line) and discarding (dash-dotted and dotted lines) initial transients.

generation. Conversely, Ro effects first appear on low Ro cases, and then on larger Ro cases as the distance of travel increases. Therefore, at fixed root location, the lift on low AR cases, which correspond to low Ro values, is always driven by competing AR and Ro effects. On the contrary, the lift on larger AR cases is first driven by AR effects and then by competing AR and Ro effects as rotational effects propagate from root to tip with the distance of travel. On lower AR cases, Ro effects can never compensate for detrimental AR effects, resulting in lower lift. On larger AR cases, beneficial AR effects are dominant during initial transients but are counteracted by Ro effects at large distance of travels, here again resulting in lower lift.

The effect of initial transients on lift optimality can further be revealed by averaging the lift force in the post-transient phase, i.e. discarding intitial transients. Figure 19 compares the lift coefficient computed discarding the first 120° of revolution with that taking into account initial transients. It can be seen that when initial transients are discarded, no clear lift optimum emerges (lift oscillates between $AR = 2$ and 4). This is also shown with data from [16] where the lift is averaged over $171° < \phi < 261°$, leading to a plateau between $AR = 2$ and 4 (also see results on rotating wings in [15]). Revolving wing studies in the litterature generally focus on the post-transients phase of the revolving motion, i.e. where the LEV inboard reaches a quasi-steady state. Therefore, while some of our conclusions are in line with these studies (e.g. [32]), and in particular with recent observations by [16] who equally concluded on the role of aspect ratio and Rossby number effects, our results indicate a clear optimal lift that we demonstrate to arise from competing mechanisms with competing time scales.

Finally, it is important to note that our results pertain to hovering flight and the results do not necessarily imply that an aspect ratio between 3 and 4 will

maximize lift for forward flight. In particular, forward speed increases Rossby number which is detrimental to LEV stability [35]. Thus, in relation with the above discussion on transient effects, the amplitude and reduced frequency at which the wing flaps may also be important parameters for lift optimization during forward flight (i.e. they can be adapted to avoid lift drop due to LEV shedding). On the other hand, producing lift is more challenging during hovering flight as it relies on the rotational motion alone, and it seems reasonable to suppose that wing configurations and kinematics have evolved to satisfy this more restrictive contraint than that imposed by forward flight conditions. We thus view our calculations as supporting [1] hypothesis of a convergent high-lift solution across a range of scales in nature, but further work is required to determine whether species employing higher or lower aspect ratios do so for lift optimality, or for other reasons.

4 Conclusions

We numerically computed the flow past an 45° angle of attack rectangular wing undergoing a 180° revolving motion at a Reynolds number based on the wing chord and the velocity at the radius of gyration of 577. We analyzed the lift and flow structure obtained for different aspect ratios at constant wing root position, and for different aspect ratios and Rossby numbers at constant Rossby number and aspect ratio respectively.

For higher aspect ratio wings ($AR > 4$) with root located on the axis of rotation, the flow is characterized by an inboard quasi-steady region, where a robust conical spanwise LEV develops, and an outboard unsteady region, where the LEV bursts into smaller scale structures and reorients chordwise, along with the tip vortex (figure 20a). The transition between quasi-steady and unsteady regions appears to be driven by local Rossby number r/c and occurs around $r/c = 3$, which is consistent with previous studies [1, 15]. For $r/c < 3$, the LEV does not reach the trailing edge because of a limited growth rate. For $r/c > 3$, the LEV reaches the trailing and cross-wake interactions occur, which promotes shedding.

If the radial position of the wing tip R_2/c approaches or deceeds $r/c = 3$ (with R_1/c sufficiently below three), then the transition between quasi-steady and unsteady regions is pushed towards lower values of r/c (figure 20b). In this case, induced velocity at the wing tip promotes LEV bursts despite enhanced rotational effects at local values of r/c below three. Spanwise velocity component of the tip vortex on the upper surface of the wing is here oriented inboard and opposes outboard velocity due to rotational effects and spanwise gradients in flow speed [4]. A detailed analysis of this mechanism is provided in [28] for an $AR = 2$ wing with $R_1/c = 0.5$.

If the radial position of the wing root R_1/c approaches or exceeds $r/c = 3$ (with R_2/c sufficiently greather than three), then the transition between quasi-steady and unsteady regions is pushed towards higher values of r/c (figure 20c). In this case, the inboard flow is not stabilized due to enhanced rotational effect

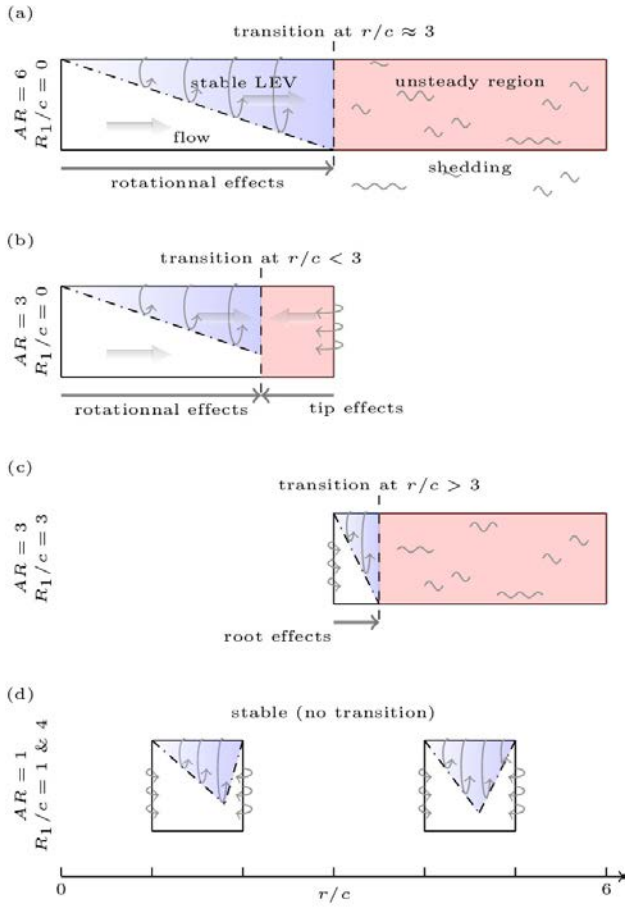

Figure 20: Schematic of the flow topology for representative cases. The transition between quasi-steady inboard region and unsteady outboard region in (a), (b) and (c) relies on (a) rotational effects, (b) rotational and tip effects and (c) root effects. No transition is observed in (d) where root and tip effects tend to stabilize the flow.

but exhibits a quasi-steady pattern due to induced velocity at the wing root. The influence of the root vortex on flow stablity is limited to a small portion in the vicinity of the wing root, comparable to that observed for translating wings.

Accordingly, all cases exhibit a wake composed of a relatively smooth RV inboard and burst LEV/TV structures outboard, except $AR = 1$ cases where the proximity of RV and TV tends to stabilize the flow (figure 20d). These differences between inboard and outboard patterns reflect the asymmetry associated with Ro and are expected to be reduced as Ro increases, $Ro \to \infty$ being the translating wing case.

Overall, these results suggest that effects of aspect ratio on the flow structure are different at low and high Rossby numbers according to whether LEV stability is promoted or not. Despite this, it is shown that variations in mean lift due to changes in aspect ratio do not significantly depend on Rossby number and, reciprocally, that variations in mean lift due to changes in Rossby number do not significantly depend on aspect ratio. In particular, our results support recent observations by [16] in that the mean lift decreases and increases monotonically with Ro and AR respectively. As a consequence, varying the aspect ratio for an impulsively started wing revolving around its root, such that the Rossby number also increases, results in two competing effects that lead to an optimum lift for AR between 3 and 4, which matches the aforementioned convergent solution found in nature. Furthermore, we show that Ro and AR effects have different time scales such that initial transients play a key role in lift optimality, which we verify to occur for AR between 3 and 4 for a range of flapping amplitudes relevant to real world observations. The existence of lift optimality is also demonstrated at a lower Reynolds number typical of fruitflies ($Re = 115$, see supplementary material, figure C) where viscous effects are hypothesized to alter mechanisms of LEV stabilization [36].

Yet, it is important to mention that a revolving motion constitutes a simplified model of a half stroke of a hovering flapping wing. Specifically, our model allows to extract the role of initial transients on the dynamics of the three-dimensional flow and on the resulting lift, discarding any dependency to flapping wing kinematics (i.e. discarding the effect of kinematic parameters related to pronation/supination phases, which greatly complexify the problem). Thus, flapping kinematics should be considered in the future to confirm lift optimality as a function of aspect ratio and Rossby number for flapping wings. In particular, attention should be paied as to how three-dimensional transient mechanisms are affected by wing kinematics, including initial wing acceleration.

Finally, while global parameters AR and Ro are convenient to parameterize the problem and reveal salient features of revolving wing aerodynamics, we showed that three-dimensional, transient mechanisms are correlated with the local Rossby number. Thus, because the distribution of local Rossby number along the span depends on the wing planform, future studies are needed to understand the precise role of wing planform on the three-dimensional mechanisms at play.

This article has additional data provided as electronic supplementary mate-

rial (figures A, B and C). We declare we have no competing interests.

The simulations were performed using the Extreme Science and Engineering Discovery Environment (XSEDE), which is supported by National Science Foundation grant number TG-CTS120005. This work was also partly supported by fundings from the Fondation ISAE-Supaero.

The authors are grateful to Dr. Sebastian Liska for helpful discussions on numerical implementation of the immersed boundary and Lattice Green's Function method, and to Pr. Michael Dickinson for insightful comments on the manuscript.

References

[1] Lentink D, Dickinson MH. 2009 Rotational accelerations stabilize leading edge vortices on revolving fly wings.. *J. Exp. Biol.* **212**, 2705–2719.

[2] Dickinson M, Lehmann F, Sane S. 1999 Wing rotation and the aerodynamic basis of insect flight.. *Science* **284**, 1954–1960.

[3] Taira K, Colonius T. 2009 Three-dimensional flows around low-aspect-ratio flat-plate wings at low Reynolds numbers.. *J. Fluid Mech.* **623**, 187–207.

[4] Jardin T, David L. 2014 Spanwise gradients in flow speed help stabilize leading-edge vortices on revolving wings.. *Phys. Rev. E* **90**, 013011.

[5] Jardin T, David L. 2015 Coriolis effects enhance lift on revolving wings.. *Phys. Rev. E* **91**, 031001.

[6] Ellington CP, den Berg CV, Willmott AP, Thomas AL. 1996 Leading-edge vortices in insect flight.. *Nature* **384**, 626–630.

[7] Chen D, Kolomenskiy D, Liu H. 2017 Closed-form solution for the edge vortex of a revolving plate.. *J. Fluid Mech.* **821**, 200–218.

[8] Jardin T. 2017 Coriolis effect and the attachment of the leading edge vortex.. *J. Fluid Mech.* **820**, 312–340.

[9] Limacher E, Morton C, Wood D. 2016 On the trajectory of leading-edge vortices under the influence of Coriolis acceleration.. *J. Fluid Mech.* **800**, R1.

[10] Garmann DJ, Visbal MR. 2014 Dynamics of revolving wings for various aspect ratios.. *J. Fluid Mech.* **748**, 932–956.

[11] Wolfinger M, Rockwell D. 2014 Flow structure on a rotating wing: effect of radius of gyration.. *J. Fluid Mech.* **755**, 83–110.

[12] Wolfinger M, Rockwell D. 2015 Transformation of flow structure on a rotating wing due to variation of radius of gyration.. *Exp. Fluids* **56**, 1–18.

[13] Harbig RR, Sheridan J, Thompson MC. 2013 Reynolds number and aspect ratio effects on the leading-edge vortex for rotating insect wing planforms.. *J. Fluid Mech.* **717**, 166–192.

[14] Carr ZR, DeVoria AC, Ringuette MJ. 2015 Aspect-ratio effects on rotating wings: circulation and forces.. *J. Fluid Mech.* **767**, 497–525.

[15] Kruyt JW, van Heijst GF, Altshuler DL, Lentink D. 2015 Power reduction and the radial limit of stall delay in revolving wings of different aspect ratio.. *J. R. Soc. Interface* **12**, 20150051.

[16] Lee Y, Lua K, Lim T. 2016 Aspect ratio effects on revolving wings with Rossby number consideration.. *Bioinspiration Biomim* **11**, 056013.

[17] Widmann A, Tropea C. 2015 Parameters influencing vortex growth and detachment on unsteady aerodynamic profiles.. *J. Fluid Mech.* **773**, 432–459.

[18] Liska S, Colonius T. 2016a A fast lattice Green's function method for solving viscous incompressible flows on unbounded domains.. *J. Comp. Phys.* **316**, 360–384.

[19] Liska S, Colonius T. 2016b A fast immersed boundary method for external incompressible viscous flows using lattice Green's functions.. *arXiv:1604.01814v1 [physics.flu-dyn].*

[20] Peskin C. 1972 Flow patterns around heart valves: a numerical method.. *J. Comp. Phys.* **10**, 252–271.

[21] Roma A, Peskin C, Berger M. 1999 An adaptive version of the immersed boundary method.. *J. Comp. Phys.* **153**, 509–534.

[22] Taira K, Colonius T. 2007 The immersed boundary method: a projection approach.. *J. Comp. Phys.* **225**, 2118–2137.

[23] Roache PJ. 1998 Verification and validation in computational science and engineering.. *Hermosa.*

[24] Carr ZR, Chen C, Ringuette MJ. 2013 Finite-span rotating wings: three-dimensional vortex formation and variations with aspect ratio.. *Exp. Fluids.* **54**, 1444.

[25] Garmann DJ, Visbal MR, Orkwis PD. 2013 Three-dimensional flow structure and aerodynamic loading on a revolving wing.. *Phys. Fluids* **25**, 034101.

[26] Ellington CP. 1984 The aerodynamics of insect flight I-VI.. *Philos. Trans. R. Soc. Lond. B Biol. Sci.* **305**, 1–181.

[27] Jeong J, Hussain F. 1995 On the identification of a vortex.. *J. Fluid Mech.* **285**, 69–94.

[28] Medina A, Jones A. 2016 Leading-edge vortex burst on a low-aspect-ratio rotating flat plate.. *Phys. Rev. Fluids* **1**, 044501.

[29] Helmbold H. 1942 Der unverwundene ellipsenflugel als tragende flanche.. *Jahrbuch 1942 der Deutch Luftfahrtforsch* pp. I111–I113.

[30] Anderson J. 1999 *Aircraft Performance and Design.* McGraw-Hill.

[31] Phillips N, Knowles K, Bomphrey RJ. 2017 Petiolate wings: effects on the leading-edge vortex in flapping flight.. *Interface Focus* **7**, 20160084.

[32] Smith DT, Rockwell D, Sheridan J, Thompson M. 2017 Effect of radius of gyration on a wing rotating at low Reynolds number: A computational study.. *Phys. Rev. Fluids* **2**, 064701.

[33] Wojcik C, Buchholz J. 2014 Vorticity transport in the leading-edge vortex on a rotating blade.. *J. Fluid Mech.* **743**, 249–261.

[34] Sane S, Dickinson M. 2001 The aerodynamic effects of wing rotation and a revised quasi-steady model of flapping flight.. *J. Exp. Biol.* **205**, 1087–1096.

[35] Harbig RR, Sheridan J, Thompson MC. 2014 The role of advance ratio and aspect ratio in determining leading-edge vortex stability for flapping flight.. *J. Fluid Mech.* **751**, 71–105.

[36] Shyy W, Liu H. 2007 Flapping wings and aerodynamic lift: the role of leading-edge vortices.. *AIAA J.* **45**, 2817–2819.